IEEE Access
Multidisciplinary ⋮ Rapid Review ⋮ Open Access Journal

Received January 15, 2021, accepted January 24, 2021, date of publication February 1, 2021, date of current version February 12, 2021.

Digital Object Identifier 10.1109/ACCESS.2021.3055803

Cross-Dataset Multiple Organ Segmentation From CT Imagery Using FBP-Derived Domain Adaptation

JUN HUANG[1], XUE LI[1], JING WANG[1], XIAXIA YU[1], LIANGJIA ZHU[4], YING ZHAN[5], YI GAO[1,2,3], AND CHUAN HUANG[6,7]

[1]School of Biomedical Engineering, Health Science Center, Shenzhen University, Shenzhen 518060, China
[2]Peng Cheng Laboratory, Shenzhen 518066, China
[3]Marshall Laboratory of Biomedical Engineering, Shenzhen 518060, China
[4]Pathovision Inc., Shenzhen, China
[5]Hainan Remote Molecular Imaging Diagnostic Center, Haikou, China
[6]Department of Psychiatry, Stony Brook University, Stony Brook, NY 11794, USA
[7]Department of Radiology, Stony Brook University, Stony Brook, NY 11794, USA

Corresponding author: Yi Gao (gaoyi@szu.edu.cn)

This work was supported in part by the Department of Education of Guangdong Province under Grant 2017KZDXM072, in part by the National Natural Science Foundation of China under Grant 61601302, in part by the Shenzhen Peacock Plan under Grant KQTD2016053112051497, and in part by the Faculty Development Grant of Shenzhen University under Grant 2018009.

ABSTRACT Multi-organ segmentation from whole-body computed tomography (CT) scans has gained increasing research interest over recent years. While the learning-based segmentation algorithm has lately achieved tremendous success, the need for detailed annotation of multiple organs further increases the manual burden. With a limited number of annotated volumetric datasets, it would be beneficial to apply the trained model from such a set to CT images acquired from other sites with different scanners. Nevertheless, the discrepancy among training and testing images significantly deteriorates segmentation performance. While there are many domain adaptation efforts, in this work we proposed a filtered back-projection based algorithm for performing domain adaptation for CT imagery. An optimal CT reconstruction kernel was obtained by minimizing the disparity between two images. Furthermore, since the Gaussian kernel is an eigen-function of the Fourier transformation, the adaptation computation was proven to be simple linear filtering. The proposed method was tested and compared with multiple methods to demonstrate improvement by employing such a model/theory-based adaptation approach. The proposed method, used in conjunction with a common convolutional neural network, such as the U-Net or V-Net, with or without the domain adaptation, achieves high accuracy in a multiple-organ segmentation task. Approximately 30% of data was used for training, 70% was used for testing, and an average dice of 0.88 was achieved in 8 organs.

INDEX TERMS Multi-organ segmentation, domain adaptation, filtered back-projection.

I. INTRODUCTION

When performing radiological diagnosis, image-guided radiotherapy, treatment assessment, and extracting contours of various organs/tissues are of critical importance amongst other factors. Due to shape variability and lack of boundary features in certain regions, contouring abdominal organs can be time consuming. In addition, detailed abdominal organ segmentation on CT is a challenging task in both human performance and automatic algorithms. There are several reasons for this, including the low contrast of soft tissues, morphological complexity of the structures, and large intra-/inter-variations. To address the problem of CT image organ segmentation, various approaches have been proposed, such as the atlas based methods. An atlas-based segmentation algorithm performs deformable registration of the image to previously segmented ones. Besides, atlas-based segmentation is also used as a component in other algorithms pipelines to extract the target region coarsely [1]–[4]. Its performance is affected by factors which include representative atlas selection, selection of deformation registration methods, and fusion of different organ labels. Moreover, the variances in

The associate editor coordinating the review of this manuscript and approving it for publication was Hengyong Yu.

This work is licensed under a Creative Commons Attribution-NonCommercial-NoDerivatives 4.0 License.
For more information, see https://creativecommons.org/licenses/by-nc-nd/4.0/

abdominal organs are often much greater compared to other organs, rendering it a much more challenging situation for the deformable registration. While increasing a training atlas may increase the segmentation accuracy and robustness, there is usually a limit above which the performance plateaus. Also, the calculation time tends to increase with respect to the number of atlas.

Recently, the machine learning approach has been adopted by many researchers and has achieved much success. Learning-based methods that rely on big data have been applied to the segmentation problems with medical images [5]–[9]. Deep convolutional neural networks (CNN) [10]–[13] and full convolutional networks (FCN) [14] have shown to have high performances when applied to semantic segmentation of natural images and medical images [15], [16]. Currently, many segmentation tasks have been adopting the deep learning-based strategy (e.g. segmentation of the brain and other structures) [17]–[20]. Among them, the U-Net type of structure was adopted by many researchers [21]. The U-Net can use a relatively small amount of data to learn a very robust model. In [22], researchers proposed the 3D U-Net network architecture to process 3D medical images.

Despite the tremendous progress that has been made with automatic or semi-automatic segmentation methods, training and segmenting across different datasets are still very challenging tasks. Although many CNNs have achieved good results with various datasets and challenges [23], [24], the results obtained in these studies are often limited to training and prediction data acquired under the same condition. When training on one data set and testing on another data set collected by different methods/parameters, it is often difficult to obtain satisfying results.

Indeed, studies [25], [26] have found that, in many application scenarios, the test data is only related to the training data while the distributions are significantly different. In order to solve the problem of inconsistent distribution of training data and testing data, commonly used methods are the ones based on feature representations (Haar features, gradients, colors, histograms, etc.). In [27], [28], the authors proposed a new method based on histogram matching. At present, feature-based methods have achieved good performance in most cross-dataset segmentation and classification problems.

Regarding CT images, different CT manufacturers and clinical sites may use different methods when reconstructing images. Reconstruction methods may have different kernel functions, resulting in large variations in the visual appearance and texture of acquired CT images. For example, the difference between two sets of CT images is very evident. This work contained sets of CT images. Abdominal images were smoother relative to [what was being compared] and the whole-body CT images were sharper despite a certain level of noise (see details in Section II-A). Therefore, for CT images intended for cross-dataset testing, using a method that is based only on feature representation for domain adaptation does not significantly improve test results, we proposed a method of domain adaptation based on the principle of CT reconstruction.

We believe the main contributions of this work are:

It is common in the image analysis tasks that the segmentation model is trained on a set of images, while during its application, the model is used on a different set of images obtained from a different site/machine. In particular, for CT images, two sets of images may not be reconstructed with the same kernel. In this scenario, the segmentation performance deteriorates significantly if the original model is applied directly. To address this issue, we propose a filtered back projection (FBP)-derived domain adaptation. The FBP-derived domain adaptation method automatically adjusts the discrepancy between different CT data sets, and improves the robustness and generalization ability of the pretrained segmentation model.

The 3D-patch based learning and segmentation framework loses the spatial context information. This causes the problem that certain non-related region with similar texture may be extracted by the patch-based segmentation. To address such an issue, an efficient whole-body registration-based atlas approach is adopted. Specifically, the whole-body registration guides the region of targets to the desired location and successfully removes the false negative regions caused by the patch-based CNN segmentation.

II. METHOD AND MATERIALS

It is possible to obtain good and consistent results by using organ segmentation from CT images, especially when the training and testing data are from the same cohort. However, if the testing data are (1) of different pathological status from the training data and/or (2) reconstructed with different reconstruction parameters, the testing and training data will be significantly different. This results in the degradation of segmentation performance. In order to mitigate the problem caused by the discrepancy between training and testing data, various domain adaptation methods have been proposed. These methods aimed to transform the distribution of the testing data to that of the training data.

The general adaptation may omit certain domain knowledge and thus cannot obtain better effect. When the CT images were constructed with different reconstruction kernels, an analytical method could be derived to map them. Herein, we proposed a new method for cross-dataset multiple organ segmentation from CT imagery using FBP-derived domain adaptation. The overall workflow of our method is shown in Figure 1.

A. DATASETS

Two representative sets of CT data used in this study are shown in Figure 2. D1 is the VISCERAL dataset. It contains 20 whole-body CT volumes and 20 abdominal CT volumes [29]–[31]. The whole-body CT volumes have no contrast enhancement and the resolution is $0.977^2-1.405^2\times 3$ (mm). The abdominal CT volumes have contrast enhancement and resolution is $0.604^2-0.793^2 \times 3$ (mm). In this

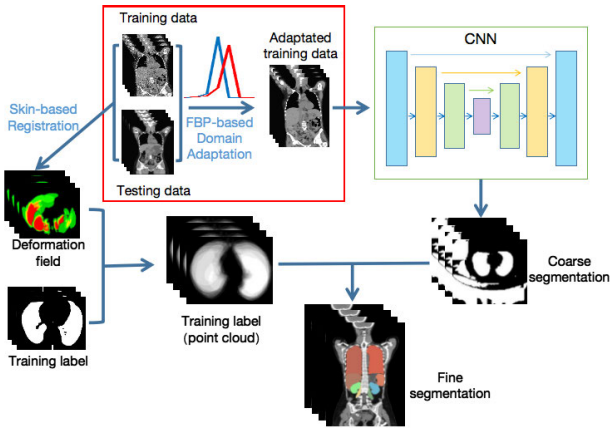

FIGURE 1. The overall workflow of the proposed method. The filtered back-projection (FBP)-derived domain adaptation is performed on the training and testing data. The adapted testing image is then fed to the trained model for segmentation. In cases where the training images are altered by the domain adaptation step, the neural network is re-trained, and then the segmentation is performed. Furthermore, a whole-body registration is used to fuse the contextual information to alleviate the short-sighted issues brought by the patch-based segmentation. This is fused with the CNN predicted segmentation for the final result.

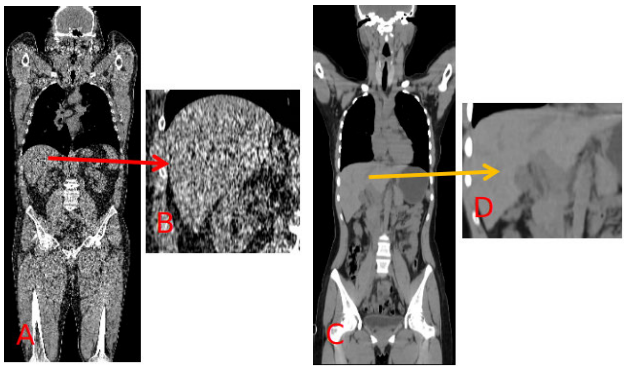

FIGURE 2. Two images from the D1 dataset (A, B) and the D2 dataset (C, D). All slices here used the same window/level setting: window=350 and level = 40. (A) shows a D1 image with a zoom-in version (B), highlighting the high-frequency texture in the liver region. (C) shows a D2 image with a zoom-in version (D). Apparently, D1 images have more high-frequency noise compared to D2, and learning from one to segment the other is the main challenge.

dataset, the Left Lung, Right Lung, Left Kidney, Right Kidney, Left Psoas Muscle, Right Psoas Muscle, Liver, Spleen were manually contoured, and then all contours were used for training. D2 consists of 92 whole-body CT volumes scanned with United Imaging uCT510 scanner. This dataset was used for testing in this work. The D1 dataset is from public domain and has the ground truth annotated. For our own dataset, the masks were drawn manually by masters students (using the software 3D Slicer) and validated by a senior radiologist (Dr. Y. Zhan in the author list) with more than 10 years of experiences. Our aim was to train the multi-organ segmentation model using D1 and apply the segmentation on D2.

B. NEURAL NETWORK TRAINING AND PREDICTION

In order to demonstrate the main contribution of this work, which is the domain adaptation derived from FBP, the backbone neural network used here is kept as simple as possible.

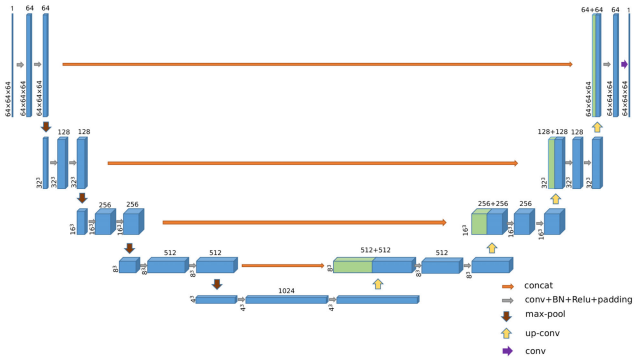

FIGURE 3. The architecture of the convolutional neural network for organ segmentation.

To that end, a patch based 3D U-Net, whose structure is shown in Figure 3 is used. Indeed, the simple yet effective U-Net provides satisfying results in a large range of segmentation publications. On the other hand, such a backbone network could be changed to others, as was done in the testing and comparison sections.

To train the network, 40 volumes and manually annotated organ labels were used. During the training phase, the patches were obtained by sampling around the labeled area of the organ; i.e., each training patch containing at least one pixel in any of the target organ/tissue. Then, in order to segment a test image $T : \mathbb{R}^3 \rightarrow \mathbb{R}$, regions $R_i \subset \mathbb{R}^3$ of the same size as the training patches were randomly sampled from the test image according to a uniform distribution. For each test image, n image patches were extracted for prediction. The image patches corresponding to the sampled area were denoted as:

$$q_i(x) = T(x)|_{R_i}, \quad i = 1, \ldots, n \tag{1}$$

Each image patch was inputted to the trained network model for prediction. Each pixel in the patch obtained a probability value between [0, 1]. The closer the probability value was to 1, the more likely it was that the pixel belonged to the target structure. The probability map of each image patch was expressed as:

$$r_i = Model(q_i), \quad i = 1, \ldots, n \tag{2}$$

Integrating the probability maps of n image patches, the global probability map of pixels at various positions x in the image T belonging to the target organ was computed as:

$$p(x) = \sum_{i=1}^{n} r_i(x) \tag{3}$$

Finally, we denoted the image predicted by the network as $K = Model(T)$.

C. FBP-DERIVED DOMAIN ADAPTATION

The above method provided a good result within the same dataset [21], [32]. However, because different CT datasets may be collected using different reconstruction and acquisition methods, the distributions of different datasets were very

different, as shown previously in Figure 2. Therefore, before feeding training data into the network, we used a domain adaptation method to adjust for image differences. As a result, the adjusted training data and testing data distribution were as consistent as possible. Recently, several domain adaptation methods have been developed to mitigate such discrepancies between the training and testing datasets [33]–[35].

In this work, the CT FBP-reconstruction theory was used to design a CT-specific domain adaptation. FBP is a commonly used algorithm for CT reconstruction. In it, the design of the filtering kernel was one of the key components, which significantly affected the appearance of the result. One of the key factors affecting various CT images was the choice of different kernel functions.

To proceed, we denote the sinogram from which the CT image was reconstructed as $G(\omega, \theta)$, and denote the reconstructed image as $f(x, y)$. The FBP reconstruction can be written as:

$$f(x,y)=\int_0^{\pi}\int_{-\infty}^{+\infty} G(\omega,\theta)e^{j2\pi\omega(x\cos\theta+y\sin\theta)}|\omega|d\omega d\theta \tag{4}$$

According to Fourier's slice theorem

$$G(\omega,\theta)=[F(u,v)]|_{u=\omega\cos\theta, v=\omega\sin\theta} \tag{5}$$

where $|\omega|$ represents the filter function that is to be multiplied by a window function to adjust the image quality. The ideal filter $|\omega|$ is a V-shaped filter function with an infinite frequency band and the integral divergence in the infinite integration interval. According to the Perry-Wiener criterion, this ideal filter is not achievable [36]. The common approach is to use a rectangular window function to limit the ideal filter, cut off the high frequency part, and only keep the low frequency band. This gives the well-known Ram-lak filter [37]. In what follows we denoted the Ram-Lak filter as

$$R(\omega)=\left\{\begin{pmatrix}|\omega| \text{ for } |\omega|\le\omega_c\\ 0 \text{ otherwise}\end{pmatrix}\right. \tag{6}$$

where ω_c is the cut-off frequency.

A different choice of kernel gives a different image appearance. Due to the frequency response feature of the Shepp-Logan kernel, the reconstructed images have more high-frequency textures, like those in Figure 2A and Figure 2B. On the other hand, Hamming window reconstructed images are smoother, as shown in Figure 2C and Figure 2D. Therefore, the domain adaptation to match these two kinds of the dataset should utilize the intrinsic link between them, instead of generic histogram/style matching approaches.

To achieve that, in theory, one could simulate the sinogram from one CT image, and perform the reconstruction using another kernel to match the texture characteristics of the other. However, the reconstruction parameter, such as the kernel size, is not always available (for example being stored in the DICOM header). Additionally, as derived below, one does not have to go through the tedious project-then-back-projection steps. Instead, exploiting the eigen-function property of the Fourier transformation, the above process can be achieved using an efficient convolution with optimal kernel searching.

More explicitly, kernels with different smoothness could be approximated by multiplication of the Ram-Lak filter with a Gaussian kernel of different width. For example, the Shepp-Logan function can be approximated as S_G:

$$S_G(\omega)=R(\omega)\times g_s(\omega)=\frac{R(\omega)}{\sqrt{2\pi}}e^{-\frac{\omega^2}{2s^2}} \tag{7}$$

where $g_s(\omega)$ is the zero-mean Gaussian kernel with s being the optimal width defined by:

$$s=\arg\min_{\sigma}\int\left(\frac{R(\omega)}{\sqrt{2\pi}}e^{-\frac{\omega^2}{2\sigma^2}}-S(\omega)\right)^2 d\omega \tag{8}$$

Similarly, we use such framework to approximate the Hamming filter function as H_G:

$$H_G(\omega)=R(\omega)\times g_s(\omega)=\frac{R(\omega)}{\sqrt{2\pi}}e^{-\frac{\omega^2}{2s^2}} \tag{9}$$

with s defined by:

$$s=\arg\min_{\sigma}\int\left(\frac{R(\omega)}{\sqrt{2\pi}}e^{-\frac{\omega^2}{2\sigma^2}}-H(\omega)\right)^2 d\omega \tag{10}$$

Moreover, the reason for adopting such approximation lies in the fact that the Gaussian kernel is the eigen-function of the Fourier transformation. This significantly simplifies the computation. Indeed, an image reconstructed using the Hamming filter function can be written as:

$$\begin{aligned}&\int_0^{\pi}\int_{-\infty}^{+\infty} G(\omega,\theta)e^{j2\pi\omega(x\cos\theta+y\sin\theta)}H(\omega)d\omega d\theta\\ &\approx\int_0^{\pi}\int_{-\infty}^{+\infty} G(\omega,\theta)e^{j2\pi\omega(x\cos\theta+y\sin\theta)}H_G(\omega)d\omega d\theta\\ &=\int_0^{\pi}\int_{-\infty}^{+\infty} G(\omega,\theta)e^{j2\pi\omega(x\cos\theta+y\sin\theta)}\times|\omega|e^{-2\pi^2\sigma^2\omega^2}d\omega d\theta\end{aligned} \tag{11}$$

Let:

$$u=\omega\cos\theta\ v=\omega\sin\theta, \tag{12}$$

we have:

$$\begin{aligned}&\int_0^{\pi}\int_{-\infty}^{+\infty} G(\omega,\theta)e^{j2\pi\omega(x\cos\theta+y\sin\theta)}\times|\omega|e^{-2\pi^2\sigma^2\omega^2}d\omega d\theta\\ &=F^{-1}\left[\int_{-\infty}^{+\infty}\int_{-\infty}^{+\infty} f(x,y)e^{j2\pi(ux+vy)}dxdy\right.\\ &\quad\left.\times\int_{-\infty}^{+\infty}\int_{-\infty}^{+\infty} e^{-2\pi^2\sigma^2(u^2+v^2)}dxdy\right]\\ &=F^{-1}[F(u,v)\times Z(u,v)]\\ &=f(x,y)*z(x,y)\end{aligned} \tag{13}$$

As detailed above, $H(\omega)$ represents the Hamming filter used in the CT image reconstruction, $H_G(\omega)$ is an approximation of the Hamming filter, and $z(x, y)$ is a two-dimensional Gaussian function. Therefore, the reconstruction

of CT images can use Gaussian functions convolution reconstructed images to approximately adjust the filter function, thus controlling image quality.

Indeed, the final formulation of the domain adaptation turned out to be as simple as a Gaussian smoothing. Yet it is more than linear smoothing. Instead, this is due to the usage of the FBP-theory derived method as well as the eigenfunction property of the Gaussian kernel for the Fourier transformation.

As shown in Equation (10) above, we find the optimal kernel factor which mapped one image to the other. To that end, it is necessary to find two corresponding regions in the two CT volumes, after which the optimal filtering parameters can be used to match the two regions. Nonetheless, identifying two corresponding regions before performing image segmentation is a challenging task; i.e., it is necessary to first segment the target (e.g., liver) from the new image, and then match the liver texture in the new image to that of the testing image, however, tissue heterogeneity may further complicate the problem. Hence, identifying two corresponding regions inside certain organs/tissue may be challenging.

Air region, on the other hand, is a good choice. Indeed, the air region is homogeneous with pre-determined Hounsfield unit(HU) and may be the easiest to capture across different images. Consequently, we took two air regions in the two CT volumes with a size of A^3 voxels where A=50 was empirically determined. These two air regions were denoted as $f_U(x, y, z)$ and $f_S(x, y, z)$.

Following Equation (13), a Gaussian kernel G_a was used to convolve with the original image to generate an image D closer to the target image, where a is the optimal standard deviation minimizing:

$$a = \arg\min_{\sigma} \int (f_U(x, y, z) * G_\sigma - f_S(x, y, z))^2 \, dxdydz \quad (14)$$

In order to determine the optimal scalar a, a gradient free optimization method such as bisection method could be used. After that, the domain-adapted version D of the image U can be computed as simple as:

$$D = G_a * U \quad (15)$$

D. BODY MASK REGISTRATION DRIVEN PRIOR CONSTRUCTION

The patch-based method used above can effectively focus on the target organ. Moreover, it puts much less burden on the GPU memory. Compared to the 2D based approaches, it utilizes the information in the third dimension, which is critical for medical images. This method has limitations: during training, the contextual information, and in potentially losing the position information of the target structure due to the size limitation of the patch. Therefore, we adopted an atlas-based method to provide spatial information [38], [39]. Since the patch-based CNN above already gives good segmentation in the target′s vicinity, the only problem lies in that certain remote regions with similar texture information may be included in the output. Therefore, we do not need state-of-the-art atlas method to give very precise registration result. Instead, we rely on the registration, providing the approximate location. A whole-image deformable registration may be affected by variations in other structures ranging from CT bed to image artifacts. In contrast, registration between two body masks can resist to various interference factors and is computationally effective. Consequently, it resulted in a suitable option.

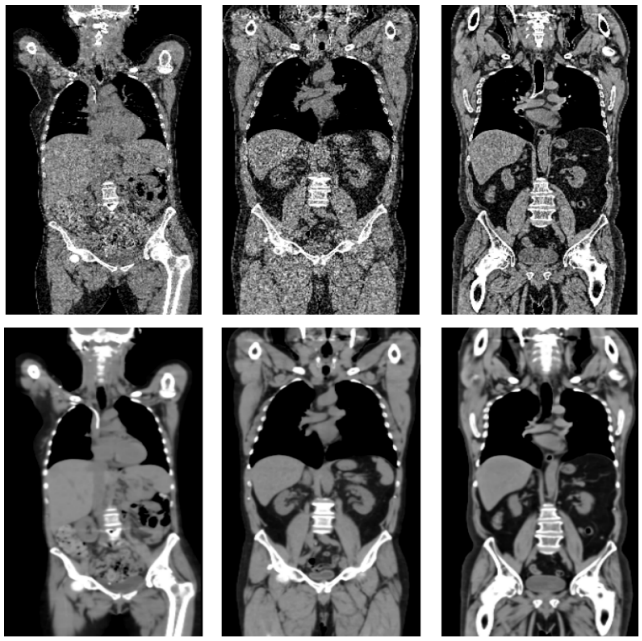

FIGURE 4. The top row represents the original images of the three patients from D1 data set; The bottom row shows the three corresponding results after FBP-derived domain adaptation.

We first segmented the body (the interface between the human body and the air) from both images to be registered. We then assigned a value of 1 to all locations with a CT value greater than -500 HU in the image, and assigned a value of 0 to locations with a CT value less than -500 HU. The obtained binary image includes the target area (body) and irrelevant areas (scanning bed, etc.). To remove extraneous areas, we kept the largest connected component. After that, the 0-regions inside the 1-region were filled to remove the air-filling cavities. Finally, we obtained a binary map $P_i : \mathbb{R}^3 \rightarrow \{0, 1\}; (i = 1, 2, \ldots, m)$ of the body region. The label of the organ of each image was expressed as $L_i : \mathbb{R}^3 \rightarrow \{0, 1, 2, \ldots, n\}, i = 1, 2, \ldots, m$ where 0 indicated the background and non-zero labels were used for various organs. Without loss of generality, we randomly selected an image of the organ label, say, L_1, and the body mask P_1 corresponding to this image as the standard template. Then we used affine registration to map the binary images $P_2, P_3, \ldots, P_m$ to the binary image P_1 of the standard template so as to obtain a diffeomorphic mapping $F_i : \mathbb{R}^3 \rightarrow \mathbb{R}^3 (i = 2, 3, \ldots, m)$. The labels of the target organs of these images could be transformed by F_i^{-1} to pull back to the common domain as $\widetilde{L_i} = F_i^{-1}(L_i), (i = 2, 3, \ldots, m)$. Next, we superimposed

them as $O = \sum_{i=2}^{m} \widetilde{L}_i$ to obtain a representative map O of the target organ label.

As in Equation (15), after obtaining the domain-adapted training image D, it was re-entered for training which updated the network model. The atlas method above then formed a representative map of the target organ O of the test image T. Finally, the segmentation result was computed as $L = O \times K$.

E. TRAINING CONFIGURATIONS AND IMPLEMENT DETAILS

The proposed algorithm was implemented in the Tensorflow framework on the Ubuntu18.04 (64 Bit) platform with a Titan XP graphic card with 12GB of memory. We used a learning rate of 10^{-4} for 10000 training epochs (which has been proven to be sufficient for the convergence of the modules in the experiments) and saved the network parameters. In each training batch, we fed 20 pieces of 64 × 64 × 64 voxels image patch to the network. In addition, we used the Dice Coefficient (Dice) [40], [41], Jaccard similarity coefficient (Jaccard) [42], [43] and sensitivity [44], [45] to measure the coverage of the segmentation result and ground truth:

$$Dice = \frac{2|V_p \cap V_{gt}|}{|V_p| + |V_{gt}|} \tag{16}$$

$$Jaccard = \frac{|V_p \cap V_{gt}|}{|V_p \cup V_{gt}|} \tag{17}$$

where V_p and V_{gt} represented the volume of the predicted region and the ground-truth region, respectively.

III. EXPERIMENT

Experiments were conducted to demonstrate the performances of the proposed method. In Section III-A and III-B, we detailed the choice for the size of the patch and air region. Then, in Section III-C, we directly applied the learned model to the testing images without any domain adaptation. Hence, in Section III-D, the commonly used histogram-based domain adaptation was used. The results of some organs were improved over the vanilla version of the CNN segmentation. In Section III-E the proposed FBP-derived domain adaptation based segmentation was tested. Quantitative analysis and comparison of the results are given in Section III-F and the results based on V-Net framework are given in Section III-G as comparison for back-bone network choice.

In each experiment, 20 whole-body CT images and 20 abdominal CT from D1 were used for training. In each of them, eight organs, including left lung, right lung, liver, spleen, left kidney, right kidney, the left psoas muscle (LPM), the right psoas muscle (RPM), were manually contoured by radiologist. The test dataset (D2) consisted of 92 whole-body CT images from PET-CT examinations. In this work, in order to maintain the consistency of data resolution, all volumes were re-sampled to 1.5 × 1.5 × 1.5mm/voxel.

A. SELECTION OF PATCH SIZE

We have tested various choices for patch sizes, ranging in {16,32,48,64,128}. Figure 5 shows the segmentation results of various organs using different patch sizes with the vanilla 3D U-Net (evaluated by Dice coefficient). As can be seen from the comparison, when the size is 64 × 64 × 64 voxels, the segmentation results appear to be the best. Since this choice is not the key concern of the present work, in the following experiments, we fixed the patch size at 64 × 64 × 64 voxels for consistent training and segmentation.

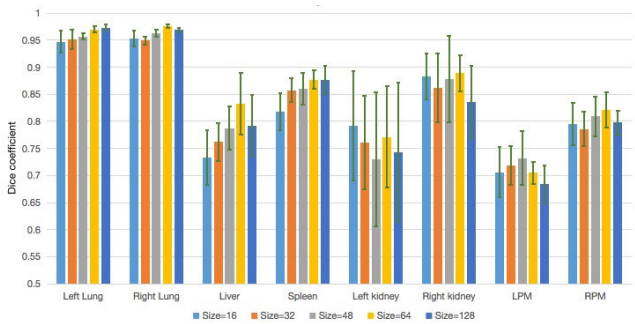

FIGURE 5. Segmentation results of organs using different patch sizes. Without using any domain adaptation, patch size is the only varying factor. By trying different patch sizes, it was observed that patch size of 64 gives the best segmentation result. Therefore, in the subsequent experiments, it's fixed at 64.

B. SELECTION OF AIR REGION SIZE

In addition, we compared the effect of the size of the air region defined at the end of Section II-C on the liver. Before training the network, we selected air regions of different sizes {5, 10, 30, 50, 80, 100} in the training data and the testing data to obtain the FBP-derived domain adapted training image. Then we trained the corresponding network separately. Figure 6 shows the prediction results of the pre-trained network for air regions of different sizes. It can be seen that the Dice changes gradually after the air region size is approximately 50 × 50 × 50 voxels. Considering it may be difficult to obtain continuous air regions with a size greater than 50 in some volume data, we fixed the size of the air region to 50 × 50 × 50 voxels in subsequent experiments.

C. MULTI-ORGAN SEGMENTATION WITHOUT DOMAIN ADAPTATION

In this experiment, the training images were directly fed into the U-Net(Section II-B) without domain adaptation. The best performance in the segmentation of the eight target organs was achieved in the right lung, with an average Dice of 0.976 and an average Jaccard of 0.953. In contrast, the worst performance (LPM) reached an average Dice of 0.705, and an average Jaccard of 0.546. As shown in Figure 7, while the segmentation of the lungs seems acceptable, the spleen, the left, and right kidneys were all poorly segmented.

D. MULTI-ORGAN SEGMENTATION WITH HISTOGRAM-BASED DOMAIN ADAPTATION

Since there is a high discrepancy between the training and testing datasets, adjusting the distributions of the two datasets is a common approach for domain adaptation. Therefore,

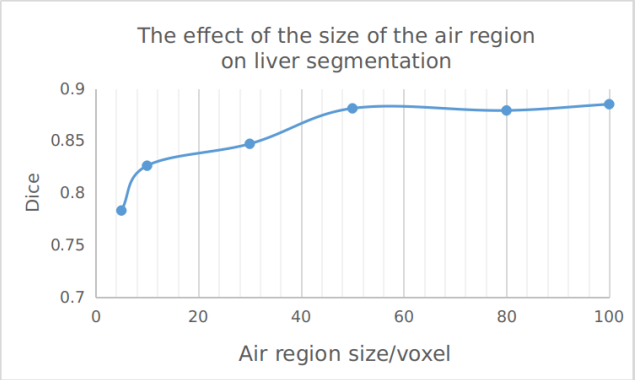

FIGURE 6. The effect of the air region size on liver segmentation. We select air regions of different sizes on the D1 and D2 data sets to test its effect. When the air region is too small, it does not contain enough samples to compute a representative distribution from which one can infer the optimal kernel. On the other hand, when the region is too large, it is difficult to obtain a complete cubic air region. It was observed that the performance was good and stable when the size is 50 × 50 × 50. Therefore, in the following experiments, the size of the air region is fixed to 50.

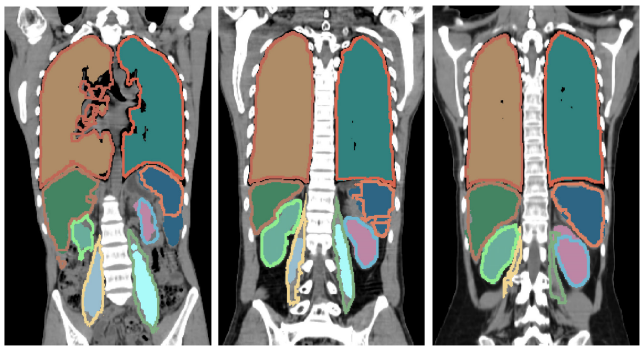

FIGURE 7. Performances without domain adaptation on three randomly picked cases. Results of different coronal slices in three cases. The solid masks are the ground truth while the contours are the prediction results. The algorithm under-segmented the spleen in the left and middle panels, and it also under-segmented the left kidney in the right panel.

such adaptation was performed before the training, i.e. the training image was adjusted so that its grayscale distribution matches that of the testing data. The adapted training images were then fed into CNN (Section II-B). The highest Dice result was obtained for the right lung, with an average Dice of 0.972. The highest Jaccard result was also obtained for the right lung, with an average Jaccard of 0.946.

On the other hand, the average Dice of the right kidney was the lowest, at only 0.567, and the average Jaccard of the right kidney was the lowest, at only 0.457. As evident by comparing Figure 8 with Figure 7, even though the better segmentation was achieved for the liver, the results for the lung (L/R) and the kidney (L/R) deteriorated. This suggests that matching the global distribution without investigating the specific image patterns may, in fact, worsen the performance.

E. MULTI-ORGAN SEGMENTATION WITH PROPOSED METHOD

In this section, we used our FBP-derived domain adaptation method to adjust the training image to the testing images.

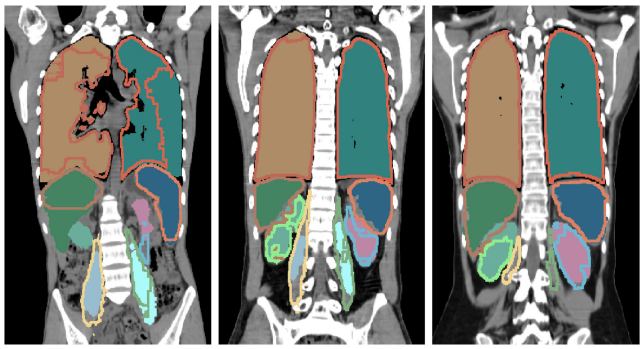

FIGURE 8. Segmentation with histogram-based domain adaptation on the same subjects as above. Results of different coronal planes in three cases. The solid masks are the ground truth while the contours are the prediction results. It can be seen that after the commonly used histogram based adaptation, the segmentation was getting poorer, for example in the lung, kidney, and other organs. This is due to the fact that the texture discrepancy cannot be adjusted well.

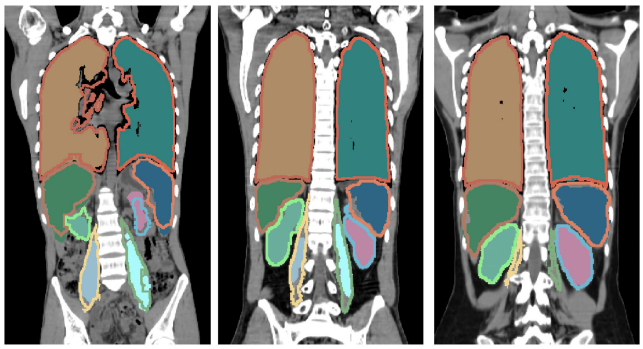

FIGURE 9. Performances with FBP-derived domain adaptation in same subjects as above. Results of different coronal planes in three cases. The solid masks are the ground truth while the contours are the prediction results. The proposed method performs better in each organ on each image.

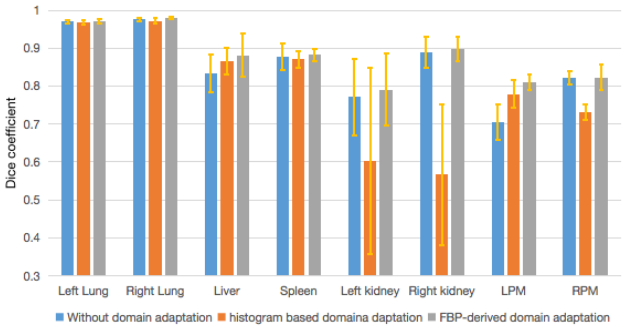

FIGURE 10. The average Dice of the three methods. The yellow vertical line indicates the standard deviation. The proposed method achieves the overall best performance on all targets, especially the liver and LPM.

The results are shown in Figure 9. Comparing this to Figure 7 and Figure 8, it can be seen that the results improved, especially for the small targets, such as the spleen and kidney.

F. QUANTITATIVE ANALYSIS OF THE RESULTS

While the segmentation results are visually presented in the previous sub-sections, in this section we conducted the quantitative analysis and comparisons. The Dice coefficients of various tests are summarized in Table 1 and Figure 10. Table 1 summarizes the Jaccard coefficients and sensitivities

TABLE 1. Comparison of the Dice±standard deviation /Jaccard /sensitivity of various organs.

	Without domain adaptation	Histogram based domain daptation	FBP derived domain adaptation
L Lung	$0.97 \pm 0.004/0.942/\mathbf{0.991}$	$0.969 \pm 0.006/0.939/0.979$	$\mathbf{0.971} \pm 0.005/\mathbf{0.945}/0.984$
R Lung	$0.976 \pm 0.004/0.953/0.992$	$0.972 \pm 0.007/0.946/0.977$	$\mathbf{0.979} \pm 0.003/\mathbf{0.958}/\mathbf{0.992}$
Liver	$0.833 \pm 0.05/0.717/0.759$	$0.865 \pm 0.035/0.764/0.902$	$\mathbf{0.881} \pm 0.057/\mathbf{0.792}/\mathbf{0.905}$
Spleen	$0.877 \pm 0.034/\mathbf{0.782}/0.892$	$0.871 \pm 0.022/0.772/\mathbf{0.943}$	$\mathbf{0.882} \pm 0.017/0.776/0.905$
L kidney	$0.771 \pm 0.101/0.667/0.739$	$0.602 \pm 0.245/0.51/0.584$	$\mathbf{0.791} \pm 0.094/\mathbf{0.679}/\mathbf{0.74}$
R kidney	$0.889 \pm 0.042/0.804/0.875$	$0.567 \pm 0.186/0.457/0.511$	$\mathbf{0.898} \pm 0.033/\mathbf{0.82}/\mathbf{0.93}$
LPM	$0.705 \pm 0.047/0.546/\mathbf{0.943}$	$0.779 \pm 0.036/0.639/0.916$	$\mathbf{0.811} \pm 0.02/\mathbf{0.683}/0.941$
RPM	$0.821 \pm 0.018/\mathbf{0.697}/0.932$	$0.731 \pm 0.021/0.576/0.948$	$\mathbf{0.823} \pm 0.033/0.68/\mathbf{0.942}$

TABLE 2. P-value with proposed method for various organs.

	L Lung	R Lung	Liver	Spleen	L kidney	R kidney	LPM	RPM
Without domain adaptation vs Proposed	0.324	0.042	1.83×10^{-4}	0.158	0.188	0.24	0.003	0.898
Histogram based domain adaptation vs Proposed	0.26	0.098	0.0129	0.002	0.047	0.009	0.007	8.7×10^{-4}

TABLE 3. Comparison of the Dice±standard deviation /Jaccard /sensitivity of eight organs under different methods based on V-Net framework.

	Without domain adaptation	Histogram based domain daptation	FBP derived domain adaptation
L Lung	$0.972 \pm 0.007/0.945/\mathbf{0.982}$	$0.967 \pm 0.006/0.936/0.974$	$\mathbf{0.973} \pm 0.007/\mathbf{0.949}/0.975$
R Lung	$0.975 \pm 0.006/0.953/0.985$	$0.968 \pm 0.006/0.938/0.994$	$\mathbf{0.978} \pm 0.005/\mathbf{0.959}/\mathbf{0.992}$
Liver	$0.701 \pm 0.155/0.599/0.643$	$0.761 \pm 0.19/0.697/0.752$	$\mathbf{0.82} \pm 0.097/\mathbf{0.733}/\mathbf{0.852}$
Spleen	$\mathbf{0.873} \pm 0.042/\mathbf{0.781}/0.9$	$0.731 \pm 0.149/0.614/0.7$	$0.834 \pm 0.05/0.709/\mathbf{0.906}$
L kidney	$0.729 \pm 0.191/0.625/\mathbf{0.748}$	$0.63 \pm 0.265/0.515/0.648$	$\mathbf{0.784} \pm 0.105/\mathbf{0.679}/0.746$
R kidney	$0.738 \pm 0.091/0.574/0.917$	$0.804 \pm 0.07/0.661/\mathbf{0.923}$	$\mathbf{0.884} \pm 0.042/\mathbf{0.798}/0.915$
LPM	$0.76 \pm 0.04/0.613/0.895$	$0.767 \pm 0.162/0.687/0.823$	$\mathbf{0.837} \pm 0.036/\mathbf{0.733}/\mathbf{0.951}$
RPM	$0.796 \pm 0.045/0.666/0.9$	$0.804 \pm 0.043/0.673/0.835$	$\mathbf{0.844} \pm 0.021/\mathbf{0.731}/\mathbf{0.944}$

and shows that the proposed method achieved the highest mean Dice, Jaccard coefficient, and sensitivity for all the organs. The specificity values are all very close to 1 so they are not listed.

Furthermore, the student t-tests were used to evaluate whether the improvement brought by the proposed method was statistically significant. The t-test results are shown in Table 2. In it, we can observe that the p-values of the t-tests indicated that the right lung, liver, and LPM were significantly improved.

Most of the significantly improved organs were soft tissues. Indeed, the image texture of the soft tissues, compared to other sites such as the bone, was severely affected by the CT reconstruction configurations. The proposed method successfully addressed this issue and therefore achieved better results.

G. COMPARISON OF SEGMENTATION EFFECTS BASED ON V-NET FRAMEWORK

The V-Net [46] has achieved advanced performance in many multi-organ segmentation tasks and proposed some V-Net-based variants [47]–[49]. In this sub-section, we compared the segmentation effects on different organs without domain adaptation, histogram-based domain adaptation, and the proposed domain adaptation method under the V-Net segmentation framework. Figure 11 shows the coronal segmentation results of three random testing data under three conditions. Through the Dice coefficients and Jaccard coefficients comparison in Table 3, it can be seen that under the V-Net segmentation framework, the proposed domain adaptation method can achieve better segmentation performance in organs except the spleen. In addition, by comparing the sensitivity scores, it can be seen that the proposed domain adaptation method is more sensitive on most organs. Statistically, as evident from the p values in Table 4, the effect of segmentation was significantly improved for most of the organs above.

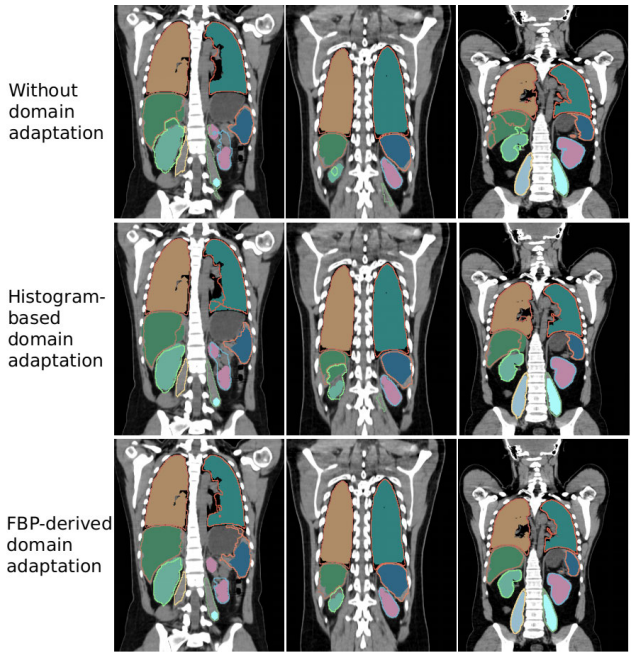

FIGURE 11. Segmentation results based on V-Net framework in different conditions. Segmentation in different coronal planes in three cases. As can be visually inspected, the main discrepancies among the three methods are located in the liver, left kidney, right kidney, spleen. The solid masks are the ground truth while the contours show the prediction result.

H. SWAPPING TRAINING DATASET AND TESTING DATASET

In this section, we used the D2 dataset as the training data and the D1 dataset as the testing data, and performed

TABLE 4. P-value with proposed method for various organs based on V-Net framework.

	L Lung	R Lung	Liver	Spleen	L kidney	R kidney	LPM	RPM
Without domain adaptation vs Proposed	0.173	0.006	8.2×10^{-4}	0.051	0.003	4.53×10^{-4}	3.59×10^{-4}	0.002
Histogram based domain adaptation vs Proposed	0.009	2.71×10^{-4}	0.008	3.88×10^{-4}	5.57×10^{-5}	9.93×10^{-4}	0.264	0.0175

TABLE 5. Comparison of the Dice±standard deviation /Jaccard /sensitivity when the training dataset is interchanged with the testing dataset.

	Without domain adaptation	Histogram based domain adaptation	FBP derived domain adaptation
L Lung	$0.978 \pm 0.004/0.947/0.987$	$0.971 \pm 0.006/0.94/0.982$	$\mathbf{0.982} \pm 0.003/\mathbf{0.953}/\mathbf{0.992}$
R Lung	$0.981 \pm 0.005/0.956/\mathbf{0.99}$	$0.963 \pm 0.009/0.941/0.976$	$\mathbf{0.984} \pm 0.003/\mathbf{0.964}/0.989$
Liver	$0.809 \pm 0.116/0.705/0.827$	$0.837 \pm 0.08/0.721/0.861$	$\mathbf{0.862} \pm 0.057/\mathbf{0.783}/\mathbf{0.877}$
Spleen	$0.83 \pm 0.05/0.714/0.805$	$0.771 \pm 0.104/0.695/0.786$	$\mathbf{0.851} \pm 0.048/\mathbf{0.762}/\mathbf{0.894}$
L kidney	$0.748 \pm 0.182/0.658/0.726$	$0.79 \pm 0.167/0.734/0.803$	$\mathbf{0.826} \pm 0.105/\mathbf{0.785}/\mathbf{0.857}$
R kidney	$0.764 \pm 0.074/0.744/0.778$	$0.805 \pm 0.063/0.783/0.826$	$\mathbf{0.873} \pm 0.054/\mathbf{0.828}/\mathbf{0.902}$
LPM	$0.772 \pm 0.08/0.716/0.781$	$0.746 \pm 0.172/0.674/0.747$	$\mathbf{0.824} \pm 0.079/\mathbf{0.798}/\mathbf{0.831}$
RPM	$0.806 \pm 0.067/0.752/0.864$	$0.827 \pm 0.08/0.796/0.876$	$\mathbf{0.859} \pm 0.036/\mathbf{0.827}/\mathbf{0.894}$

segmentation experiments for multiple organs in three cases without domain adaptation, histogram-based domain adaptation, and the proposed domain adaptation. Here, we still used the U-Net framework, and the comparison of Dice coefficients, Jaccard coefficients and sensitivity are shown in Table 5. In the segmentation performance of each organ, it can be seen that the segmentation results of the proposed method also got significantly improved.

IV. CONCLUSION

Herein, we propose a filtered back-projection (FBP) theory based algorithm for performing domain adaptation for CT images. The proposed domain adaptation method effectively mitigates the discrepancy among various datasets due to the kernel used in CT reconstruction. This new approach used in conjunction with a common convolutional neural network, such as the U-Net, achieves higher accuracy in multiple-organ segmentation tasks than the original setting. The proposed method was compared with multiple other methods to demonstrate the improvement by employing the adaptation component. It is emphasized that we do not claim the overall framework here to be superior. Instead, we believe combining the proposed FBP-derived domain adaptation would significantly improve the original segmentation accuracy. Further research should extend such a model-based domain adaptation approach to other imaging systems and cross-modality adaptations.

APPENDIX

FILTER BACK PROJECTION

In the filtered back-projection reconstruction algorithm, the design of the filter is the key. The ideal filter is a V-shaped function with infinite frequency band, whose integral diverges due to the infinite support, and cannot be realized. Therefore, the existing reconstruction methods perform windowing on the kernel functions by only retaining the low frequency part. The commonly used reconstruction kernel functions are Ram-Lak filter (Figure 12A), Shepp-Logan filter (Figure 12B), Hamming filter (Figure 12C), Hanning filter, etc.

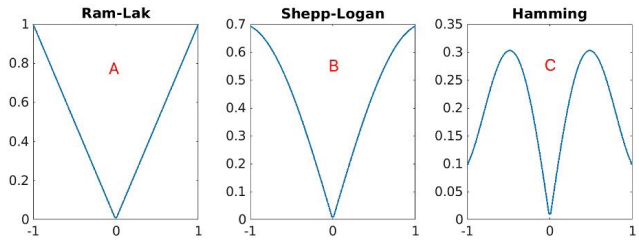

FIGURE 12. Three filtering functions commonly used in CT reconstruction. (A) The ideal filter function is truncated with a rectangular window to obtain the Ram-Lak filter function $R(\omega)$. (B) The Ram-Lak filter function is truncated with a sinc function to obtain the Shepp-Logan filter function $S(\omega)$. (C) The Ram-Lak filter function is truncated with the Hamming window to obtain the Hamming filter function $H(\omega)$.

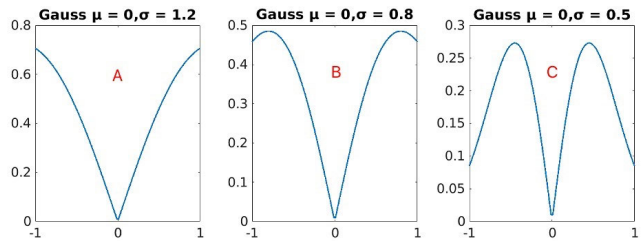

FIGURE 13. Multiplication between Ram-Lak filter and Gaussian function with different standard deviations, to approximate various kernels in Figure 12. When $\sigma = 1.2$, the generated kernel function A is similar to Figure 12B, when $\sigma = 0.5$, the generated kernel function C is similar to Figure 12C.

In the proposed method, we construct the optimal Gaussian kernel function to perform the domain adaptation on the CT image. Thanks to the eigen property of the Gaussian function, this is equivalent to using the new reconstruction kernel function to reconstruct the CT image. This is shown in Figure 13.

ACKNOWLEDGMENT

The authors would like to thank Thomas Hagan for proofreading the final manuscript. *(Jun Huang and Xue Li contributed equally to this work.)*

REFERENCES

[1] Y. Zhou and J. Bai, "Multiple abdominal organ segmentation: An atlas-based fuzzy connectedness approach," *IEEE Trans. Inf. Technol. Biomed.*, vol. 11, no. 3, pp. 348–352, May 2007.

[2] R. Wolz, C. Chengwen, K. Misawa, K. Mori, and D. Rueckert, "Multi-organ abdominal CT segmentation using hierarchically weighted subject-specific atlases," in *Proc. Int. Conf. Med. Image Comput. Comput.-Assist. Intervent.*, vol. 15, 2012, pp. 10–17.

[3] C. Chu, M. Oda, T. Kitasaka, K. Misawa, M. Fujiwara, Y. Hayashi, Y. Nimura, D. Rueckert, and K. Mori, "Multi-organ segmentation based on spatially-divided probabilistic atlas from 3D abdominal CT images," in *Proc. Int. Conf. Med. Image Comput. Comput.-Assist. Intervent.*, vol. 16, 2013, pp. 165–172.

[4] R. P. Burke, Z. Xu, C. P. Lee, R. B. Baucom, B. K. Poulose, R. G. Abramson, and B. A. Landman, "Multi-atlas segmentation for abdominal organs with Gaussian mixture models," *Proc. SPIE*, vol. 9417, Mar. 2015, Art. no. 941707.

[5] K. Z. Mao, P. Zhao, and P.-H. Tan, "Supervised learning-based cell image segmentation for P53 immunohistochemistry," *IEEE Trans. Biomed. Eng.*, vol. 53, no. 6, pp. 1153–1163, Jun. 2006.

[6] Z. Iscan, A. Yüksel, Z. Dokur, M. Korürek, and T. Ölmez, "Medical image segmentation with transform and moment based features and incremental supervised neural network," *Digit. Signal Process.*, vol. 19, no. 5, pp. 890–901, Sep. 2009.

[7] S.-H. Huang, Y.-H. Chu, S.-H. Lai, and C. L. Novak, "Learning-based vertebra detection and iterative normalized-cut segmentation for spinal MRI," *IEEE Trans. Med. Imag.*, vol. 28, no. 10, pp. 1595–1605, Oct. 2009.

[8] J. Ma, L. Lu, Y. Zhan, X. Zhou, M. Salganicoff, and A. Krishnan, "Hierarchical segmentation and identification of thoracic vertebra using learning-based edge detection and coarse-to-fine deformable model," in *Proc. Int. Conf. Med. Image Comput. Comput.-Assist. Intervent.*, 2010, pp. 19–27.

[9] T. Kohlberger *et al.*, *Automatic Multi-organ Segmentation Using Learning-Based Segmentation and Level Set Optimization*. Berlin, Germany: Springer, 2011.

[10] G. Papandreou, L.-C. Chen, K. P. Murphy, and A. L. Yuille, "Weakly- and semi-supervised learning of a deep convolutional network for semantic image segmentation," in *Proc. IEEE Int. Conf. Comput. Vis. (ICCV)*, Dec. 2015, pp. 1742–1750.

[11] X. Zhou, R. Takayama, W. Song, X. Zhou, T. Hara, and H. Fujita, "Automated segmentation of 3D anatomical structures on ct images by using a deep convolutional network based on end-to-end learning approach," *Proc. SPIE*, vol. 10133, Feb. 2017, Art. no. 1013324.

[12] H.-C. Shin, H. R. Roth, M. Gao, L. Lu, Z. Xu, I. Nogues, J. Yao, D. Mollura, and R. M. Summers, "Deep convolutional neural networks for computer-aided detection: CNN architectures, dataset characteristics and transfer learning," *IEEE Trans. Med. Imag.*, vol. 35, no. 5, pp. 1285–1298, May 2016.

[13] P. S. Bhatia, F. Reda, M. Harder, Y. Zhan, and S. Z. Xiang, "Real time coarse orientation detection in MR scans using multi-planar deep convolutional neural networks," *Proc. SPIE*, vol. 10133, Feb. 2017, Art. no. 1013303.

[14] E. Shelhamer, J. Long, and T. Darrell, "Fully convolutional networks for semantic segmentation," *IEEE Trans. Pattern Anal. Mach. Intell.*, vol. 39, no. 4, pp. 640–651, Apr. 2017.

[15] M. Fayyaz, M. H. Saffar, M. Sabokrou, M. Fathy, R. Klette, and F. Huang, "STFCN: Spatio-temporal FCN for semantic video segmentation," Tech. Rep., 2016.

[16] B. Shuai, T. Liu, and G. Wang, "Improving fully convolution network for semantic segmentation," Tech. Rep., 2016.

[17] J. Bernal, K. Kushibar, D. S. Asfaw, S. Valverde, A. Oliver, R. Martí, and X. Lladó, "Deep convolutional neural networks for brain image analysis on magnetic resonance imaging: A review," Tech. Rep., 2017.

[18] J. Amin, M. Sharif, M. Yasmin, and S. L. Fernandes, "Big data analysis for brain tumor detection: Deep convolutional neural networks," *Future Gener. Comput. Syst.*, vol. 87, pp. 290–297, Oct. 2018.

[19] P. Hu, F. Wu, J. Peng, Y. Bao, F. Chen, and D. Kong, "Automatic abdominal multi-organ segmentation using deep convolutional neural network and time-implicit level sets," *Int. J. Comput. Assist. Radiol. Surg.*, vol. 12, no. 3, pp. 399–411, Mar. 2017.

[20] F. Jiang, A. Grigorev, S. Rho, Z. Tian, Y. Fu, W. Jifara, K. Adil, and S. Liu, "Medical image semantic segmentation based on deep learning," *Neural Comput. Appl.*, vol. 29, pp. 1257–1265, Jul. 2017.

[21] O. Ronneberger, P. Fischer, and T. Brox, "U-Net: Convolutional networks for biomedical image segmentation," Tech. Rep., 2015.

[22] O. Cicek, A. Abdulkadir, S. S. Lienkamp, T. Brox, and O. Ronneberger, "3D U-Net: Learning dense volumetric segmentation from sparse annotation," in *Proc. Int. Conf. Med. Image Comput. Comput.-Assist. Intervent.*, 2016, pp. 424–432.

[23] Z. Zhou, M. M. R. Siddiquee, N. Tajbakhsh, and J. Liang, "UNet++: A nested U-Net architecture for medical image segmentation," in *Deep Learning in Medical Image Analysis and Multimodal Learning for Clinical Decision Support*. 2018.

[24] Y. Han and J. C. Ye, "Framing U-Net via deep convolutional framelets: Application to sparse-view CT," *IEEE Trans. Med. Imag.*, vol. 37, no. 6, pp. 1418–1429, Jun. 2018.

[25] J. Blitzer, R. T. Mcdonald, and F. Pereira, "Domain adaptation with structural correspondence learning," in *Proc. Conf. Empirical Methods Natural Lang. Process.*, Sydney, NSW, Australia, 2006, pp. 120–128.

[26] H. Daume and D. Marcu, "Domain adaptation for statistical classifiers," *J. Artif. Intell. Res.*, vol. 26, pp. 101–126, Jun. 2006.

[27] P. Rakwatin, W. Takeuchi, and Y. Yasuoka, "Stripe noise reduction in MODIS data by combining histogram matching with facet filter," *IEEE Trans. Geosci. Remote Sens.*, vol. 45, no. 6, pp. 1844–1856, Jun. 2007.

[28] J. Rexilius, H. K. Hahn, J. Klein, M. G. Lentschig, and H.-O. Peitgen, "Multispectral brain tumor segmentation based on histogram model adaptation," *Proc. SPIE*, vol. 6514, Mar. 2007, Art. no. 65140V.

[29] O. Jimenez-del-Toro *et al.*, "Cloud-based evaluation of anatomical structure segmentation and landmark detection algorithms: VISCERAL anatomy benchmarks," *IEEE Trans. Med. Imag.*, vol. 35, no. 11, pp. 2459–2475, Nov. 2016.

[30] O. A. J. D. Toro, O. Goksel, B. Menze, H. Müller, and A. Hanbury, "VISCERAL–visual concept extraction challenge in radiology: ISBI 2014 challenge organization," in *Proc. Visceral Challenge ISBI*, 2014, pp. 6–15.

[31] O. J. D. Toro, "Quantitative analysis of medical images: Finding relevant regions-of-interest for medical decision support," Ph.D. dissertation, Université de Genève, Genève, Switzerland, 2017.

[32] M. C. Xie, X. Han, S. Luan, L. I. Fang, and C. X. Wang, "Brain tumor segmentation using convolutional neural networks feature extraction in MRI images," *J. Qufu Normal Univ.*, 2018.

[33] R. Gopalan, R. Li, and R. Chellappa, "Domain adaptation for object recognition: An unsupervised approach," in *Proc. Int. Conf. Comput. Vis.*, Barcelona, Spain, Nov. 2011, pp. 999–1006.

[34] Y. Ganin and V. Lempitsky, "Unsupervised domain adaptation by back-propagation," Tech. Rep., 2014.

[35] E. Tzeng, J. Hoffman, K. Saenko, and T. Darrell, "Adversarial discriminative domain adaptation," Tech. Rep., 2017.

[36] Y. Wei, G. Wang, and J. Hsieh, "An intuitive discussion on the ideal ramp filter in computed tomography (I)," *Comput. Math. Appl.*, vol. 49, nos. 5–6, pp. 731–740, Apr. 2005.

[37] J. Shtok, M. Elad, and M. Zibulevsky, "Direct adaptive algorithms for CT reconstruction," in *Proc. IEEE Int. Symp. Biomed. Imag., From Nano Macro*, Jun. 2009, pp. 181–184.

[38] B. C. Vemuri, J. Ye, Y. Chen, and C. M. Leonard, "Image registration via level-set motion: Applications to atlas-based segmentation," *Med. Image Anal.*, vol. 7, no. 1, pp. 1–20, 2003.

[39] Q. Wang, E. D'Agostino, D. Seghers, F. Maes, D. Vandermeulen, and P. Suetens, "Construction and validation of statistical brain atlases for atlas-based brain image segmentation," *KUL/ESAT/PSI*, vol. 18, no. 20, pp. 5691–5702, 2005.

[40] K. H. Zou, S. K. Warfield, A. Bharatha, C. M. C. Tempany, M. R. Kaus, S. J. Haker, W. M. Wells, F. A. Jolesz, and R. Kikinis, "Statistical validation of image segmentation quality based on a spatial overlap index1," *Academic Radiol.*, vol. 11, no. 2, pp. 178–189, Feb. 2004.

[41] A. P. Zijdenbos, B. M. Dawant, R. A. Margolin, and A. C. Palmer, "Morphometric analysis of white matter lesions in MR images: Method and validation," *IEEE Trans. Med. Imag.*, vol. 13, no. 4, pp. 716–724, Dec. 1994.

[42] S. Niwattanakul, J. Singthongchai, E. Naenudorn, and S. Wanapu, "Using of Jaccard coefficient for keywords similarity," in *Proc. Int. Conf. Internet Comput. Web Services*, 2013, pp. 380–384.

[43] S. Sarawagi and A. Kirpal, "Efficient set joins on similarity predicates," in *Proc. ACM SIGMOD Int. Conf. Manage. Data (SIGMOD)*, 2004, pp. 743–754.

[44] D. G. Altman and J. M. Bland, "Diagnostic tests. 1: Sensitivity and specificity," *Brit. Med. J.*, vol. 308, p. 1552, Jun. 1994.

[45] J. B. Reitsma, A. S. Glas, A. W. S. Rutjes, R. J. P. M. Scholten, P. M. Bossuyt, and A. H. Zwinderman, "Bivariate analysis of sensitivity and specificity produces informative summary measures in diagnostic reviews," *J. Clin. Epidemiol.*, vol. 58, no. 10, pp. 982–990, 2005.

[46] F. Milletari, N. Navab, and S. Ahmadi, "V-Net: Fully convolutional neural networks for volumetric medical image segmentation," *CoRR*, vol. abs/1606.04797, 2016.

[47] E. Gibson, F. Giganti, Y. Hu, E. Bonmati, S. Bandula, K. Gurusamy, B. Davidson, S. P. Pereira, M. J. Clarkson, and D. C. Barratt, "Automatic multi-organ segmentation on abdominal CT with dense V-networks," *IEEE Trans. Med. Imag.*, vol. 37, no. 8, pp. 1822–1834, Aug. 2018.

[48] C. Shen, F. Milletari, H. R. Roth, H. Oda, and K. Mori, "Multi-class abdominal organ segmentation with improved V-Nets," *Image Process.*, 2019.

[49] L. Zhang, J. Zhang, P. Shen, G. Zhu, P. Li, X. Lu, H. Zhang, S. A. Shah, and M. Bennamoun, "Block level skip connections across cascaded V-Net for multi-organ segmentation," *IEEE Trans. Med. Imag.*, vol. 39, no. 9, pp. 2782–2793, Sep. 2020.

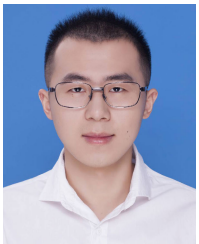

JUN HUANG received the bachelor's degree in biomedical engineering from the School of Medical Imaging, Xuzhou Medical University, in 2018. He is currently pursuing the M.S. degree in biomedical engineering with the Department of Medicine, Shenzhen University. His main research interests include organ segmentation of CT images and the blood vessel model reconstruction in ultrasound signals.

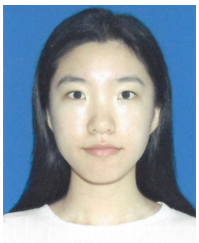

XUE LI received the B.S. degree in biomedical engineering from Jilin Medical College, Jilin, China, in 2018. She is currently pursuing the M.S. degree in Biomedical Engineering with Shenzhen University, Guangdong, China. Her main research interests include cancer screening in pathological images and detection of neural invasion.

JING WANG received the B.S. degree in aircraft environment and life support project engineering from the Nanjing University of Aeronautics and Astronautics University, Jiangsu, China, in 2012. She is currently pursuing the M.S. degree in biomedical engineering with Shenzhen University, Guangdong, China.

XIAXIA YU received the B.S. degree in mechanical engineering from National Chung Cheng University, Chiayi, Taiwan, in 2004, the M.S. degree in mechanical engineering from National Tsing Hua University, Hsinchu, Taiwan, in 2006, and the Ph.D. degree in mechanical engineering from Texas A&M University, College Station, TX, USA.

From 2008 to 2009, she was a Research Assistant with the Institute of Physics, Academia Sinica, Tapei, Taiwan. Her research interests include the development of surface processing and biological/medical treatment techniques using nonthermal atmospheric pressure plasmas, fundamental study of plasma sources, and fabrication of micro-structured or nanostructured surfaces.

Dr. Yu's awards and honors include the Frew Fellowship from Australian Academy of Science, the I. I. Rabi Prize from APS, the European Frequency and Time Forum Award, the Carl Zeiss Research Award, the William F. Meggers Award, and the Adolph Lomb Medal from OSA.

LIANGJIA ZHU received the Ph.D. degree in electrical engineering from the Georgia Institute of Technology, in 2013. He is currently a Postdoctoral Fellow with the Computer Science Department, Stony Brook University. His research interests include medical image analysis, systems and control, biological network analysis, and computer vision.

YING ZHAN graduated in medical imaging from Fujian Medical University. She is currently an Associate Chief Physician of Medical Imaging and Nuclear Medicine. She has been engaged in medical imaging and molecular imaging in the top three hospitals for more than 30 years.

YI GAO received the B.S. and M.S. degrees in biomedical engineering from Tsinghua University, and the M.S. degree in mathematics and the Ph.D. degree in biomedical engineering from the Georgia Institute of Technology. He is currently a Professor with the School of Biomedical Engineering, Shenzhen University. Prior to his current position, he was an Assistant Professor with the Departments of Biomedical Informatics, Statistics and Applied Mathematics, and Computer Science, State University of New York, Stony Brook.

CHUAN HUANG received the B.S. degree from the University of Science and Technology of China, in 2006, and the Ph.D. degree in mathematics from The University of Arizona, in 2012. He is currently an Assistant Professor of radiology and psychiatry with Stony Brook University. He was a Postdoctoral Fellow with Harvard Medical School, where he was later promoted to Instructor, before joining Stony Brook University, in 2014. His research interests include simultaneous PET/MRI, medical image reconstruction/analysis, and quantitative methods for medical imaging.